Half-Heusler phase related structural perturbations near stoichiometric composition FeZnSb

Ding-Bang Xiong [b],*, Yufeng Zhao [a]

[a] State Key Lab of Metastable Material Science and Technology, Yanshan University, Qinhuangdao 066004, PR China
[b] Department of Chemistry and Center of Material Sciences, Philipps University Marburg, Hans-Meerwein-Straße, Marburg 35032, Germany

A B S T R A C T

Half-Heusler phases XYZ (Pearson symbol cF12) are chemically versatile and rich in physical properties. The half-Heusler phase in the Fe–Zn–Sb ternary system was reported in the year 2000. In this work, two new ternary phases are identified in the vicinity of the equiatomic composition FeZnSb in the same system: $Fe_{1-x}ZnSb$ (tetragonal, space group $P4/nmm$, Pearson symbol tP6$-\delta$, $Z=2$: $a=4.1113(6)$ Å, $c=6.0127(12)$ Å for $x=0.08$ (**1**), and $a=4.1274(6)$ Å, $c=6.0068(12)$ Å for $x=0.12$ (**2**)); and $Fe_{7.87}Zn_{6.72}Sb_8$ ($Fe_{0.98}Zn_{0.84}Sb$) (**3**) (cubic, space group $Fm-3m$, Pearson symbol cF96$-\delta$, $Z=4$, $a=11.690(13)$ Å). **1** and **2** crystallize in the PbFCl-type structure, and **3** adopts a unique $2 \times 2 \times 2$ supercell of a normal half-Heusler structure. The structures of both the tetragonal and cubic phases can be described as assemblies of half-Heusler structure related subunits. Electrical resistivity measurement on the pure sample of **2** shows it has metallic-like behavior, and its thermal and magnetic properties are also characterized.

© 2011 Elsevier Inc. All rights reserved.

1. Introduction

Half-Heusler phases have the general form XYZ and crystallize in the C1$_b$ structure, which consists of four interpenetrating face-centered cubic sublattices occupied by the three atoms X, Y and Z and a vacant site. Half-Heusler phases are known to combine with a wide variety of different elements. Typically, X and Y are the alkali metal, transition metal or rare-earth metal, and Z is the main group element. Different combinations result in half-Heusler phases exhibiting a great variety of electronic states and physical properties. Most studies of the half-Heusler phases seem to simply postulate an equiatomic composition. However, experiments indicated that the phases with compositions in the vicinity of the ideal equiatomic composition can be prepared, and the deviations from the equiatomic composition made a significant difference to their physical properties, such as the electrical transport properties of TiCoSb [1] and the magnetic properties of the half-metallic ferromagnet NiMnSb [2]. Offernes and Kjekshus et al. systematically investigated the homogeneity regions of a series of half-Heusler phases [3–6]. Their results indicated that the phases calculated to be stable semiconductor (such as NiTiSn, PtTiSn and TiCoSb with valence–electron concentration

(VEC)=18) all take the euqiatomic composition, while the other phases show deviation from the euqiatomic composition [6].

Besides the influence of VEC on the composition deviation of a phase, structural perturbation can modify the electronic band structure acting as a substitute for a change in VEC [6], such as CaF$_2$-type structure in the disordered PtMnSn [7] and the $2 \times 2 \times 2$ supercell of a normal half-Heusler structure in CoMnSb [8]. We are interested in exploring the variations of structure and property with composition in half-Heusler phases. Ru–Zn–Sb system was investigated in our previous studies [9]. The equiatomic phase RuZnSb has VEC of 15, which is in the VEC gap in the structure map of half-Heusler phases [9]. Investigations showed that only the phase with a $2 \times 2 \times 2$ supercell of a normal half-Heusler structure existed in the solid solution range $Ru_{9-x}Zn_{7+x}Sb_8$ $(0 \leq x \leq 1)$ and no normal half-Heusler phase was observed. Both CoMnSb and $Ru_{9-x}Zn_{7+x}Sb_8$ $(0 \leq x \leq 1)$ adopt a $2 \times 2 \times 2$ supercell of a normal half-Heusler structure, but the ratios of the number of two different transition metals X and Y in respective ordered phases are different, namely Co$_8$Mn$_8$Sb$_8$ and Ru$_9$Zn$_7$Sb$_8$ [8,9]. In this work, as a result of our ongoing investigations on half-Heusler phases, we report the structural variation in the vicinity of the equiatomic composition in the Fe–Zn–Sb ternary system. Two new non-stoichiometric phases are identified, one is $Fe_{1-x}ZnSb$ [$x=0.08$ (**1**) and 0.12 (**2**)] with a PbFCl-type structure and the other is $Fe_{7.87}Zn_{6.72}Sb_8$ ($Fe_{0.98}Zn_{0.84}Sb$) (**3**) with a $2 \times 2 \times 2$ supercell of a normal half-Heusler structure. Physical properties for the pure sample of **2** are also characterized.

* Corresponding author. Present address: Department of Materials Science and Engineering, Kyoto University, Kyoto 606-8501, Japan.
E-mail address: xiong.dingbang@ky8.ecs.kyoto-u.ac.jp (D.-B. Xiong).

2. Experimental section

2.1. Synthesis

All samples were prepared on about 300 mg scale via high-temperature reaction of iron (99.9%), zinc (99.99%) and antimony (99.8%) in evacuated fused-silica tubes. As shown in Table 1, five reactions with three different atomic ratios of Fe:Zn:Sb were carried out, 1:1:1, 0.95:0.99:1 and 0.91:0.97:1. The loaded non-stoichiometric compositions in the reactions **II–V** were decided according to the elemental analyses and single-crystal X-ray diffraction (XRD) refinements. In reactions **I**, **II** and **III**, the samples were heated to 1273 K at a rate of 60 K/h, maintained at 1273 K for 3 h, then cooled to 873 K at a rate of 50 K/h, and maintained at 873 K for four days. The loss of Zn and Sb due to condensation outside the reaction zone was reduced by placing the reactants at the least hot site of the ampoules, and the furnace was placed on small slope to make sure the elements contact thoroughly. Thereafter the ampoules were taken out from the furnace and cooled to room temperature in air. The products from the reaction **III** were then used as precursors without any treatment in the reactions **IV** and **V**. They were annealed again at 873 K for four days in the reaction **IV** and at 570 K for two weeks in the reaction **V**.

Powder XRD patterns were recorded with an X'pert MPD diffractometer (Philips) operating in Bragg–Brentano geometry with Cu $K\alpha$ radiation. The purities were checked by comparing the experimental patterns and the theoretical patterns calculated from the single-crystal refinement results. Chemical compositions of selected crystals were examined in a scanning electron microscope (CS 4DV, CamScan) providing an energy dispersive X-ray spectrometer (EDS, Si(Li)-detector, Noran Instruments).

2.2. Crystal structure determination

Crystals of **1**, **2** and **3** were selected from the reactions **III**, **IV** and **V**, respectively, and used for single-crystal XRD analyses. The diffraction intensities were recorded with an imaging plate diffractometer (IPDS, Stoe & Cie) operating with Mo $K\alpha$ radiation ($\lambda = 0.71069$ Å) at 293(2) K. Numerical absorption corrections based on the sizes and shapes of the crystals were applied to the data sets with the programs of *X-SHAPE* [10] and *X-RED* [11]. All structures were successfully solved by applying a direct method and subsequently refined on F^2 with a full-matrix least-square algorithm with the aid of the program of *SHELXTL*, version 6.1 [12].

2.2.1. $Fe_{0.92}ZnSb$ (1) and $Fe_{0.88}ZnSb$ (2)

The extinction conditions led to the space groups of $P4/n$ (No. 85) and $P4/nmm$ (No. 129). Refinements with both space groups resulted in qualitatively identical structure models, therefore the higher symmetry space group $P4/nmm$ (No. 129) was chosen for the detailed structure analysis. At this stage the refinements for both structures converged smoothly at $R(F)$ values smaller than 5% and gave a composition of FeZnSb, and the structures were subsequently refined with anisotropic displacement parameters. Site occupancies were checked for deviations from unity by freeing the site occupancy factor (SOF) of an individual atom while the remaining SOFs were kept fixed. Iron positions in both structures were found with less than full occupancy (92% in **1** and 88% in **2**), while zinc and antimony with full occupancy. The crystal structure of FeZnSb was similar to MnZnSb [13] and was isotypic with PbFCl. As like in the refinement of MnZnSb, X-ray diffraction analysis did not allow to unambiguously determine whether iron and zinc atoms occupy only their respective sites or have a tendency for disorder. Neutron diffraction method indicated no mixed distribution of manganese and zinc [14], but magnetization measurements strongly suggested structural disorder of manganese and zinc [13,14]. In this work, based only on single-crystal XRD data, both structures were refined without mixed distribution of iron and zinc.

2.2.2. $Fe_{7.87}Zn_{6.72}Sb_8$ (3)

The structure was solved in the space group of Fm-$3m$ (No. 225) and identical with $Ru_9Zn_7Sb_8$ [9]. At this stage the refinement converged smoothly at $R(F)$ value smaller than 5% and gave a composition of $Fe_9Zn_7Sb_8$, and the structure was subsequently refined with anisotropic displacement parameters. Site occupancies were checked for deviations from unity by freeing the site occupancy factor (SOF) of an individual atom while the remaining SOFs were kept fixed. All positions are fully occupied except one of two zinc positions and one of two iron positions were found with less than full occupancy (72% for Zn1 and 86% for Fe2), resulting in the refined composition $Fe_{7.87}Zn_{6.72}Sb_8$. As like in **1** and **2**, the structure was refined without mixed distribution of iron and zinc.

Additional details concerning data collection and crystallographic data, atomic coordinates, and interatomic distances are summarized in Tables 2–4. Further details of the crystal structure

Table 1
Reaction compositions, products in the Fe–Zn–Sb System.

Sample	Loaded Fe:Zn:Sb	Conditions (T_1/T_2)[a]	Products and estimated yields[b]	Single-crystal diffraction
I	1:1:1	1273/873	95% tetragonal phase+5% β-Zn_4Sb_3	
II	0.95:0.99:1	1273/873	95% tetragonal phase+5% β-Zn_4Sb_3	
III	0.91:0.97:1	1273/873	90% tetragonal phase+10% β-Zn_4Sb_3	**1**
IV		III@873	>98% tetragonal phase	**2**
V		III@570	90% superstructure phase+10% $Zn_{1+\delta}Sb_{1-\delta}$	**3**

[a] Loaded elements were melt at temperature T_1 at first, and then annealed at temperature T_2.
[b] Percentages were estimated according to observed peak intensities in powder patterns.

Table 2
Crystallographic and technical data of the single-crystal structure refinements of the compounds in the Fe–Zn–Sb system.

	1	2	3
Formula	$Fe_{0.92}ZnSb$	$Fe_{0.88}ZnSb$	$Fe_{7.87}Zn_{6.72}Sb_8$
Space group (No.), Z	$P4/nmm$ (129), 2	$P4/nmm$ (129), 2	Fm-$3m$ (225), 4
Pearson symbol	$tP6-\delta$	$tP6-\delta$	$cF96-\delta$
a (Å)	4.1113(6)	4.1274(6)	11.690(13)
c (Å)	6.0127(12)	6.0068(12)	
V (Å^3)	101.63(3)	102.33(3)	1597.5(3)
D_c (g cm^{-3})	7.94	7.89	7.68
μ (mm^{-1})	31.43	31.21	29.93
θ_{max} (deg)	32.9	32.8	32.65
refl. coll. R(int)	1038/0.0528	998/0.1149	4331/0.1452
data/parameter	135/11	129/11	187/16
R1/wR2 [$I_o > 2\sigma(I_o)$][a,b]	0.0336/0.0337	0.0315/0.0315	0.0811/0.0850
[all data]	0.0942/0.0942	0.0864/0.0864	0.1499/0.1513
Goodness of fit (F^2)	1.296	1.308	1.320
$\Delta\rho_{min}/\Delta\rho_{max}$/e (Å^{-3})	−1.872/1.342	−1.358/2.335	−3.129/5.546

[a] $R = \sum ||F_o| - |F_c|| / \sum |F_o|$,
[b] $wR = \{\sum [w(F_o^2 - F_c^2)^2] / \sum [w(F_o^2)^2]\}^{1/2}$.

investigations can be obtained from the Fachinformationszentrum Karlsruhe, D-76344 Eggenstein–Leopoldshafen, Germany (fax: (+49) 7247 808 666; or e-mail: crysdata@fiz.karlsruhe.de) on quoting the depository numbers CSD-422233 for $Fe_{0.92}ZnSb$, CSD-422232 for $Fe_{0.88}ZnSb$ and CSD-422234 for $Fe_{7.87}Zn_{6.72}Sb_8$.

2.3. Physical property measurements

The thermal stability of the pure sample of **2** was studied in the temperature range from 570 to 1240 K using a differential scanning calorimeter (DSC, setsys 16/18, Setaram). The sample ($\approx$ 33 mg) was pressed into pellets, and then sealed in an evacuated silica ampoule which were repeatedly heated and cooled down at a rate of 0.17 K/s in order to produce an approximate thermal balanceable process.

A direct current four-probe resistivity measurement was performed on a cold-pressed bar of **2** [$(0.2 \times 0.2 \times 1.5)\ cm^3$]. Four silver wires were attached to the sample with silver epoxy, and then solidified in air. Data were recorded at 2.7 K intervals on cooling and heating in the temperature range from 30 to 300 K.

Magnetic susceptibility measurements were carried out with the aid of SQUID magnetometer (MPMS, Quantum Design). Polycrystalline sample of **2** was loaded into gelatin capsules. Temperature dependence data were collected for both zero field

cooled (ZFC) and field cooled mode (FC) between 5 and 350 K, with the applied fields of 50, 500 and 5000 Oe. The raw data were corrected for the diamagnetic contributions from both sample holder and core.

3. Results and discussions

3.1. Reaction chemistry

In the vicinity of the equiatomic composition, only the phase $Ru_{9-x}Zn_{7+x}Sb_8$ with a $2 \times 2 \times 2$ supercell of a normal half-Heusler structure was found in the solid solution range $0 \le x \le 1$ we investigated in the Ru–Zn–Sb system [9], but three different phases in the Fe–Zn–Sb system. The isothermal sections of the Fe–Zn–Sb ternary diagram at 570 K [15], 723 K [16], and 873 K [17] have been successfully studied, in which only the crystal structures of two ternary phases were reported, $FeZnSb_2$ with NiAs-type structure and equiatomic FeZnSb with a normal half-Heusler structure. Here in our work, two new ternary phases are identified in the vicinity of the equiatomic composition: tetragonal $Fe_{1-x}ZnSb$ [$x=0.08$ (**1**) and 0.12 (**2**)] and cubic $Fe_{7.87}Zn_{6.72}Sb_8$ ($Fe_{0.98}Zn_{0.84}Sb$) (**3**).

Compound **1** was obtained directly by melting elements at 1273 K and then annealing at 873 K for four days. Its powder XRD pattern (Fig. 1a) shows that the sample contains $\sim$10% Zn_4Sb_3 as impurity. Pure sample was obtained by annealing the impure sample again at 873 K for four more days (Fig. 1b). Refinement on singe-crystal XRD data of the crystal selected from the pure sample also resulted in the same PbFCl-type structure but slightly different composition $Fe_{0.88}ZnSb$ (**2**) [$Fe_{1-x}ZnSb$ with $x=0.12$]. Comparing their powder XRD patterns and compositions, we can see that the presence of impurity Zn_4Sb_3 in reaction **III** was caused by incomplete reaction, and long annealing time was necessary for preparing pure tetragonal phase. As indicated by the first two strongest peaks at 43.4° and 43.9° in powder XRD patterns, all the ternary FeZnSb phases prepared by Zhu et al. [16] were tetragonal phases identical with **1** and **2**, but no crystal structure was determined. According to their results of elemental analyses, the solid solution range of the tetragonal phase can be estimated as $Fe_{1-x}Zn_{1-y}Sb$ with $0 \le x, y \le 0.2$ at least.

Only impure sample for **3** can be obtained in our experiments (Fig. 1c). It was obtained by annealing impure sample from reaction **III** at 570 K for two weeks. Compound **3** is Fe richer than **1**, but it was invalid to improve the purity of compound **3** by the addition of elemental Fe into the reaction **V**. Annealing the pure sample from reaction **IV** did not lead to **3**. Therefore, the change of

Table 3

Atomic coordinates and equivalent displacement parameters (Å^2) for the compounds in the Fe–Zn–Sb system.

Atom	Wyckoff	x	y	z	U_{eq}[a]	Occupancy
1						
Sb	2c	1/4	1/4	0.7188(1)	0.0210(5)	1
Zn	2c	1/4	1/4	0.2651(4)	0.0297(5)	1
Fe	2a	1/4	3/4	0	0.0239(8)	0.918(14)
2						
Sb	2c	1/4	1/4	0.7226(1)	0.0112(4)	1
Zn	2c	1/4	1/4	0.2681(3)	0.0182(4)	1
Fe	2a	1/4	3/4	0	0.0130(6)	0.880(11)
3						
Sb1	8c	1/4	1/4	1/4	0.0057(7)	1
Sb2	24e	0.2707(2)	0	0	0.0097(7)	1
Zn1	4a	0	0	0	0.017(4)	0.72(6)
Zn2	24d	0	1/4	1/4	0.0138(8)	1
Fe1	4b	1/2	1/2	1/2	0.0121(19)	1
Fe2	32 f	0.1196(2)	0.1196(2)	0.1196(2)	0.0072(12)	0.86(3)

[a] U_{eq} is defined as one-third of the trace of the orthogonalized U_{ij} tensor.

Table 4

Interatomic distances (Å) in the structure of the compounds in the Fe–Zn–Sb system.

|					
1					
Sb–Fe $\times$ 4	2.6618(6)	Zn–Fe $\times$ 4	2.6012(13)	Fe–Zn $\times$ 4	2.6012(13)
Zn	2.728(2)	Sb	2.728(2)	Sb $\times$ 4	2.6618(6)
Zn $\times$ 4	2.9087(4)	Sb $\times$ 4	2.9087(4)	Fe $\times$ 4	2.9071(4)
2					
Sb–Fe $\times$ 4	2.6524(5)	Zn–Fe $\times$ 4	2.6176(10)	Fe–Zn $\times$ 4	2.6176(10)
Zn	2.730(2)	Sb	2.730(2)	Sb $\times$ 4	2.6524(5)
Zn $\times$ 4	2.9190(4)	Sb $\times$ 4	2.9190(4)	Fe $\times$ 4	2.9185(4)
3					
Sb1–Fe2 $\times$ 4	2.640(4)	Fe1–Sb2 $\times$ 6	2.681(2)	Zn1–Fe2 $\times$ 8	2.422(4)
Zn2 $\times$ 6	2.9225(3)	Fe2–Zn1	2.422(4)	Sb2 $\times$ 6	3.164(2)
Sb2–Fe2 $\times$ 4	2.6511(16)	Zn2 $\times$ 3	2.5693(15)	Zn2 − Fe2 $\times$ 4	2.5693(15)
Fe1	2.681(2)	Sb1	2.640(4)	Sb1 $\times$ 2	2.9225(3)
Zn2 $\times$ 4	2.9325(4)	Sb2 $\times$ 3	2.6511(16)	Sb2 $\times$ 4	2.9325(4)
Zn1	3.164(2)	Fe2 $\times$ 3	2.797(5)		
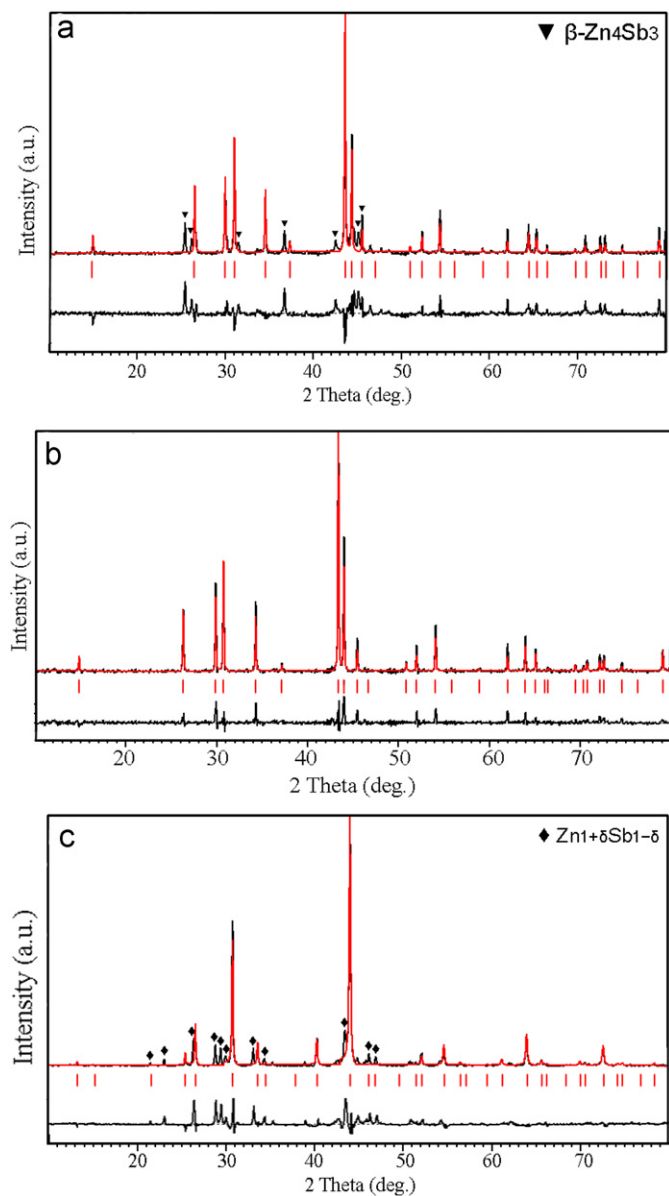
Fig. 1. Experimental (black) and calculated (red) patterns for (a) reaction **III**, (b) reaction **IV** and (c) reaction **V**. The middle red bars are calculated Bragg positions, and the bottoms are the intensity difference between experimental and calculated patterns. (For interpretation of the references to color in this figure legend, the reader is referred to the web version of this article.)

crystal structure from tetragonal phase to cubic phase was caused by composition variation, but not a phase transition.

3.2. Crystal structures

Compounds **1** and **2** crystallize in a PbFCl-type structure with similar structural features as previously reported for MnZnSb [13]. The crystal structure contains planar square iron nets (Wyckoff site $2a$) with significant indications for vacancies (8% in **1** and 12% in **2**). Such vacancies are known to exist up to 11% in MnZnSb. Each square iron net is sandwiched by two slightly fluctuant square nets of zinc and antimony positions ($2c$) (Fig. 2a and b). Zinc is in square pyramidal coordination with respect to the antimony atoms while iron atom is approximately tetrahedrally coordinated by antimony (Table 4). The c/a ratios of **1** of 1.462 and **2** of 1.455 at room temperature are much smaller than that of isotypic Fe-based superconductor LiFeAs (c/a=1.683) [18]
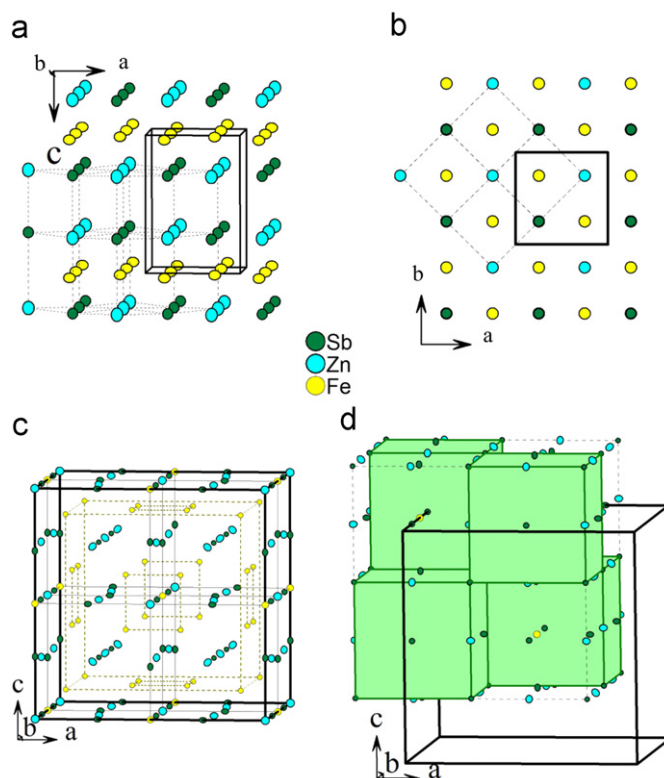

Fig. 2. Projections of the structures of the tetragonal phases (**1** and **2**) along the (a) b and (b) c axes. The dashed lines indicate the subunit relating to a half-Heusler-type structure (also see Fig. 3d). (c) The structure of **3** exhibiting a $2 \times 2 \times 2$ supercell of a normal half-Heusler structure. The dashed lines are drawn to indicate the relative positions of iron atoms. (d) The structure of **3** can also be presented as an alternation of full-Heusler-type (solid cubes) and NaCl-type structural units. The boundaries of the elementary cell at $(-1/4, -1/4, 1/4)$ are shifted relative to the origin. The solid bold lines are the unit cells.

and NaFeAs (c/a=1.782) [19] because the corrugated LiAs nets in LiFeAs and NaAs nets in NaFeAs. Because the compressed atomic arrangement along the c axis in **1** and **2**, the interatomic distances between iron atoms are expanded in the ab plane, and d(Fe−Fe)=2.9071(4) Å in **1** and 2.9185(4) Å in **2** are significantly longer than d(Fe−Fe)=2.66963(2) Å in LiFeAs and d(Fe−Fe)=2.7927(7) Å in NaFeAs. Selected interatomic distances are given in the Table 4.

Compound **3** crystallizes in the structure identical with $Ru_9Zn_7Sb_8$ [9], a $2 \times 2 \times 2$ supercell of normal half-Heusler structure, but with significant indications for vacancies in one of two zinc sites and one of two iron sites (Table 3). For convenience, hereafter in the part of structure description the vacancies will not be shown in all chemical formulas. As like $Ru_9Zn_7Sb_8$, the displacements of Sb2 and Fe2 from their ideal position in normal half-Heusler structure cause the distortions in **3**. The supercell corresponds to a coherently ordered inversion twin of half-Heusler-type subunits $Fe_{4.5}Zn_{3.5}Sb_4$ (Fig. 2c). The subunits derivate from a normal half-Heusler phase XYZ by partially replacing Y by X, namely $X_4(Y_{(6/2+4/8)}X_{4/8})Z_{(1+12/4)}$ (Fig. 3c). The structure of **3** can also be presented as an alternation of full-Heusler Fe_2ZnSb and $(FeZn_3)Sb_4$ with a NaCl-type atomic arrangement structural units (Fig. 2d).

Generally, antimony will occupy the Z sites in a half-Heusler structure because it is the main group element (Fig. 3a). However, the structure of the half-Heusler phase in the Fe–Zn–Sb system was reported as that the Z sites were occupied by transition metals (Fig. 3b) [15]. As mentioned above, the structure of **3** corresponds to a coherently ordered inversion twin of half-Heusler-type
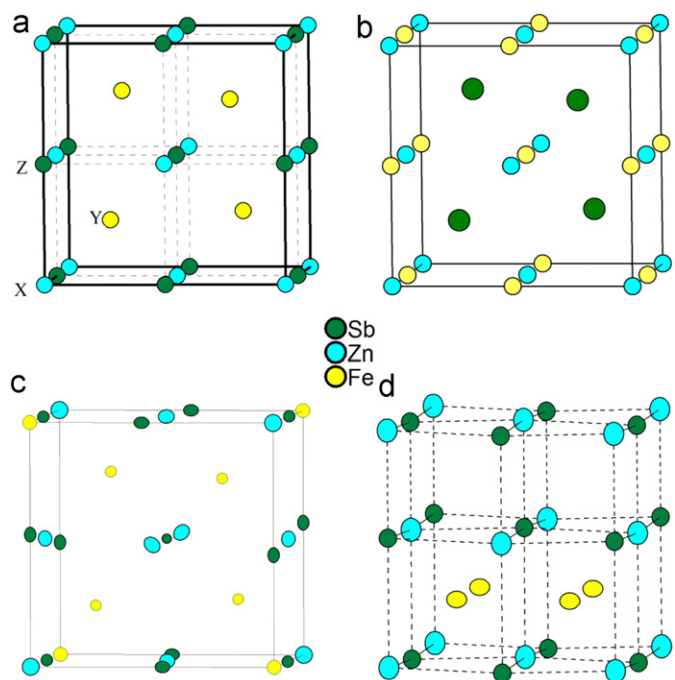
Fig. 3. (a) An ideal half-Heusler phase XYZ assuming antimony occupying the Z sites; (b) reported half-Heusler phase with transition metal occupying the Z sites; (c) half-Heusler-type subunit $Fe_{4.5}Zn_{3.5}Sb_4$ $[X_4(Y_{(6/2+4/8)}X_{4//8})Z_{(1+12/4)}]$ in **3**; and (d) half-Heusler structure related subunit with Fe_4 square in **1** and **2**.

subunits but with the modified composition $Fe_{4.5}Zn_{3.5}Sb_4$ (Fig. 3c). The structures of **1** and **2** can also be decomposed into the subunits relating to half-Heusler structure, which can be obtained by compressing the Fe_4 tetrahedron in a half-Heusler structure into a Fe_4 square in **1** and **2** (Fig. 3d). Therefore, structural relationship can be established between the structures of all three ternary phases in the vicinity of the equiatomic composition FeZnSb and the ideal half-Heusler structure. Their differences in details may be attributed to the requirement of VEC. The equiatomic phase FeZnSb has the VEC of 15 ($8_{Fe}+2_{Zn}+5_{Sb}$), and it is in the gap of the VEC map of half-Heusler phases [9]. Composition variation (such as vacancy and substitution) is the most direct way to meet the VEC requirement for a half-Heusler structure. At the same time, structural perturbation can also modify the electronic band structure acting as a substitute for a change in VEC [6]. The interplay between the composition variation and structural perturbation results in several different modified half-Heusler subunit in the Fe–Zn–Sb system.

3.3. Physical properties

Fig. 4 shows the electrical resistivity of compound **2** increases slowly with temperature increasing, indicating a metallic-like behavior. A dip at ~50 K in Fig. 4 was observed, which can be repeated in our four times measurements, and may be correlated to the change in temperature dependence of the magnetic susceptibility also observed in this range. The absolute value of electrical resistivity at room temperature is about 145 μΩ m. This magnitude is much larger than that would be expected for a metal, which may be attributed to low density of the cold-pressed specimens. As comparison, MnZnSb is semiconductor-like compound and has an activation energy of ~0.01 eV [13].

According to thermal analyses (Fig. 5) and powder XRD, compound **2** melts congruently at 1032(3) K, and partially recrystallizes upon cooling at about 20 K below the melting point. In all cases we found that part of the original **2**, if molten,
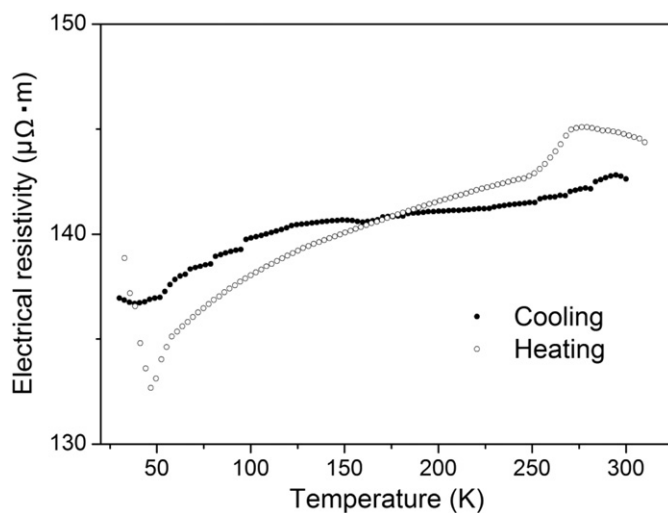

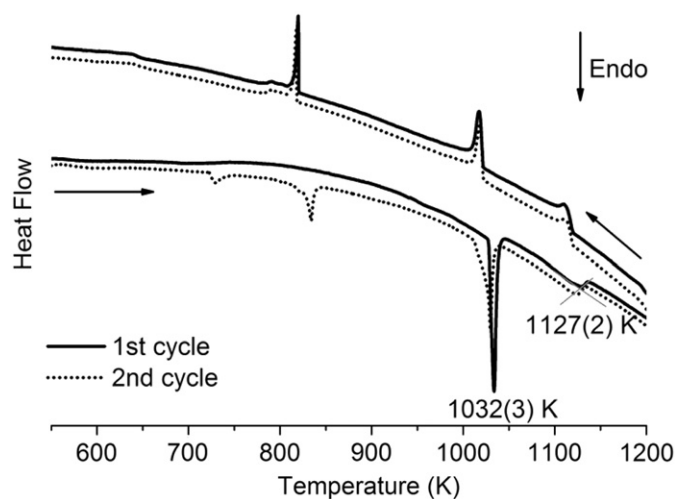**Fig. 4.** Electrical resistivity as a function of temperature for **2**.

Fig. 5. DSC curves for **2**.

decomposes into Zn_4Sb_3 and Fe_3Sb_2 (PDF card No.: 4-834), which can be confirmed by the peaks in the DSC curves [20] and also the powder XRD patterns of the samples both after the DSC analyses and quenched from 1200 K. The decomposition may be attributed to the reaction between the liquid and silica tube.

Fig. 6 shows the temperature dependence of the ZFC and FC molar magnetic susceptibility $\chi_m(T)$ of **2**. The compound shows a ferromagnetic ordering transition at ~275 K. Above 275 K, compound **2** exhibits paramagnetic behavior and $\chi_m(T)$ nicely follows the Curie–Weiss(CW) law $\chi(T)=C/(T-\theta_p)$ [21], where $C=N_A(\mu_{eff})^2/3\kappa_B=(\mu_{eff})^2/8$ is the Curie constant and θ_p is the Weiss temperature. Linear least-squares fit to this equation of the data above 280 K resulted in a Weiss temperature of $\theta_p \approx 42(10)$ K suggesting ferromagnetic interactions between the iron atoms, and an effective moment of 1.95 μ_B/Fe atom for ideal composition FeZnSb or 2.22 μ_B/Fe atom assuming 0.88 Fe atoms per formula unit as suggested by the structure refinement of **2**. This value is comparable to that of the body-centered cubic elemental iron (2.22 μ_B/Fe atom) [21].

As in the case of ZnMnSb, all available magnetic properties in references were measured under high applied field above 16 KOe, and found to be simply ferromagnetic with a relatively high Curie temperature just above 300 K [13,22,23]. We have measured the
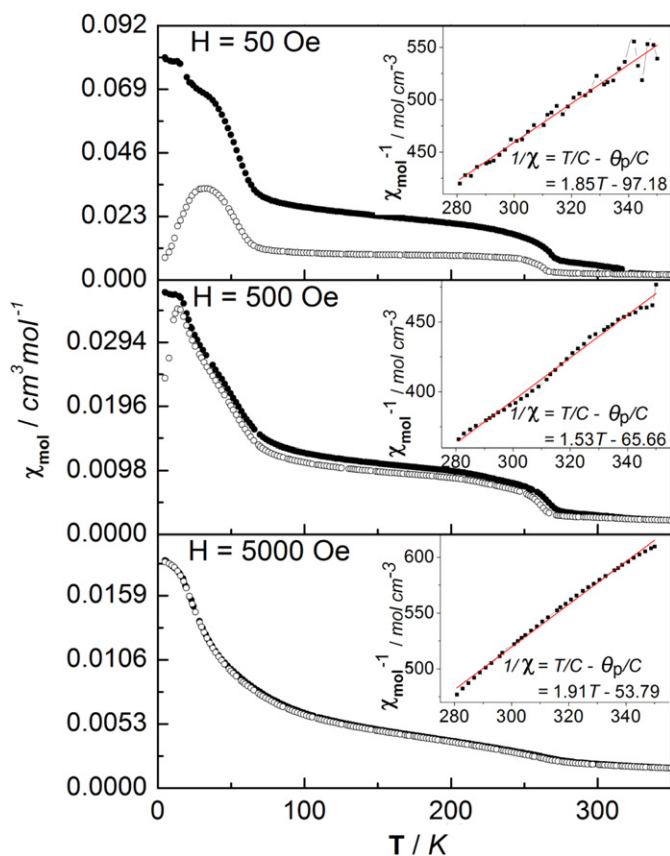
Fig. 6. Temperature-dependent magnetic susceptibility for **2** at $H=50$, 500 and 5000 Oe with zero-field-cooled ($\circ$) and field-cooled ($\bullet$) measurements. Insets show the temperature dependent inverse susceptibility above 280 K.

magnetic properties of ZnMnSb under the magnetic field as low as 50 Oe, and the results were the same with that obtained under high magnetic field in references. In contrast to ZnMnSb, the magnetic properties of **2** at low temperature are complex, and there are other two magnetic anomalies expect for the ferromagnetic transition at ~275 K. The first one is indicated by faster increasing magnetic susceptibility χ with decreasing temperature below ~70 K, which is possibly due to ferromagnetic cluster caused by structural defects. The second one is the disagreement of FC and ZFC below ~30 K under the applied field of 50 and 500 Oe, and it is a typical feature of spin-glass. $FeWN_2$ contains hexagonal iron nets and shows spin-glass or antiferromagenetic behavior at ~45 K [24]. The exact origins of these two anomalies at low temperature in **2** are not sure at present. Sample dependence of magnetic property will be useful to answer the question how the defects in crystal structure influence the magnetic property.

4. Conclusions

In summary, two new ternary phases are identified in the vicinity of the equiatomic composition FeZnSb: tetragonal $Fe_{1-x}ZnSb$ ($x=0.08$ and 0.12) and cubic $Fe_{7.87}Zn_{6.72}Sb_8$. The former crystallizes in a PbFCl-type structure, and the latter adopts a unique $2\times2\times2$ supercell of a normal half-Heusler structure. Both structures can be decomposed into half-Heusler structure

related subunits. The FeZnSb reported by Chumak et al. [15] crystallized in a normal half-Heusler-type structure, in which the Z sites are occupied by iron but not the main group element antimony. These modified half-Heusler subunits are the result of the interaction between structural perturbation and valence electron concentration.

Supporting information available

X-ray crystallographic data (CIF).

Appendix A. Supplementary materials

Supplementary materials associated with this article can be found in the online version at doi:10.1016/j.jssc.2011.03.029.

References

[1] Y. Xia, V. Ponnambalam, S. Bhattacharya, A.L. Pope, S.J. Poon, T.M. Tritt, J. Phys.: Condens. Matter 13 (2001) 1–13.
[2] B. Alling, S. Shallcross, I.A. Abrikosov, Phys. Rev. B 73 (2006) 064418.
[3] A. Neumann, L. Offernes, A. Kjekshus, B. Klewe, J. Alloys Compd. 274 (1998) 136–141.
[4] L. Offernes, A.N. Torgersen, A. Kjekshus, J. Alloys Compd. 307 (2000) 174–178.
[5] C. Walle, L. Offernes, A. Kjekshus, J. Alloys Compd. 349 (2003) 105–110.
[6] L. Offernes, P. Ravindran, C.W. Seim, A. Kjekshus, J. Alloys Compd. 458 (2008) 47–60.
[7] K. Watanabe, J. Phys. Soc. Jpn. 28 (1970) 302–307.
[8] V. Ksenofontov, G. Melnyk, M. Wojcik, S. Wurmehl, K. Kroth, S. Reiman, P. Blaha, C. Felser, Phys. Rev. B 74 (2006) 134426.
[9] D.B. Xiong, Y.F. Zhao, N.L. Okamoto, C. Pietzonka, T. Waki, H. Inui, Inorg. Chem. 49 (2010) 10536–10542.
[10] X-SHAPE (v. 2.01)-Crystal Optimization for Numerical Absorption Correction. Sote & Cie. Darmstadt (Germany), 2001.
[11] X-RED (v. 1.02)-Data Reduction Program. Stoe & Cie. Darmstadt (Germany), 2001.
[12] Sheldrick G.M. SHELXTL Programs, release version 6.10; Bruker AXS: Madison, WI, 1998.
[13] V. Johnson, W. Jeitschko, J. Solid State Chem. 22 (1977) 71–75.
[14] V.P. Dymont, G.I. Makovetskii, V.M. Ryzhkovskii, Phys. Status Solidi. (a) 107 (1988) K89–K91.
[15] I.V. Chumak, V.V. Pavlyuk, G.S. Dmytriv, J. Stepień-Damm, J. Alloys Compd. 307 (2000) 223–225.
[16] Z.X. Zhu, X.P. Su, F.C. Yin, H. Tu, C.J. Wu, J. Alloys Compd. 490 (2010) 541–547.
[17] Z.X. Zhu, X.P. Su, J.H. Wang, C.J. Wu, Y. Wu, CALPHAD 34 (2010) 98–104.
[18] M.J. Pitcher, D.R. Parker, P. Adamson, S.J.C. Herkelrath, A.T. Boothroyd, R.M. Ibberson, M. Brunelli, S.J. Clarke, Chem. Commun. (2008) 5918–5920.
[19] D.R. Parker, M.J. Pitcher, P.J. Baker, I. Franke, T. Lancaster, S.J. Blundell, S.J. Clarke, Chem. Commun. (2009) 2189–2191.
[20] G. Nakamoto, K. Kinoshita, M. Kurisu, J. Alloys Compd. 436 (2007) 65–68.
[21] C. Kittel, Introduction to Solid State Physics, seventh Ed., Wiley, Hoboken NJ, 1996.
[22] F. Ono, X. Hu, N. Fujii, K. Hayashi, N. Okada, S. Endo, T. Kanomata, Physica B 237–238 (1997) 162–163.
[23] S.-I. Mori, T. Kanomata, H. Yamauchi, S. Sakatsume, T. Kaneko, Jpn. J. Appl. Phys. 32 (Suppl. 32–3) (1993) 273–274.
[24] D.S. Bem, J.D. Houmes, H.-C. zur Loye, In: A.R. Barron, G.S. Fischman, M.A. Fury, A.F. Hepp (Eds.), MRS Symposium Proceeding, Covalent Ceramics II: Non-Oxides, Boston, 1993, vol. 327, pp. 153–162.